

**Supporting Information**  
**Critical Role of Acceptor Dopants in Designing Highly Stable and**  
**Compatible Proton-Conducting Electrolytes for Reversible Solid**  
**Oxide Cells**

Zheyu Luo, ‡<sup>a</sup> Yucun Zhou, ‡<sup>a</sup> Xueyu Hu,<sup>a</sup> Nicholas Kane,<sup>a</sup> Tongtong Li,<sup>a</sup> Weilin Zhang,<sup>a</sup> Zhijun Liu,<sup>a</sup> Yong Ding,<sup>a</sup> Ying Liu,<sup>b</sup> and Meilin Liu <sup>\*a</sup>

<sup>a</sup>School of Materials Science and Engineering, Georgia Institute of Technology, Atlanta, GA 30332-0245, USA

<sup>b</sup>Phillips 66 Company, 2331 CityWest Blvd, Houston, TX, 77042, USA

#Z.L. and Y.Z. contributed equally to the work.

\*Corresponding author: [meilin.liu@mse.gatech.edu](mailto:meilin.liu@mse.gatech.edu)

## Experimental Section

**Electrolyte Fabrication.** BaHf<sub>0.1</sub>Ce<sub>0.7</sub>R<sub>0.2</sub>O<sub>3-δ</sub> (BHCR172, R = Yb, Er, Y, Gd, Sm), and BaZr<sub>0.1</sub>Ce<sub>0.7</sub>Y<sub>0.1</sub>Yb<sub>0.1</sub>O<sub>3-d</sub> (BZCYYb1711) powders were synthesized using a solid-state reaction process. BaCO<sub>3</sub>, HfO<sub>2</sub>, ZrO<sub>2</sub>, CeO<sub>2</sub>, and R<sub>2</sub>O<sub>3</sub> were combined in appropriate molar ratios, followed by ball-milling in ethanol using YSZ milling media for 24 hours. The mixture was then dried on a hot plate to evaporate the ethanol. The well mixed powders were then pressed into large pellets, followed by multiple calcination (1100 °C for 10 h) and ball-milling steps until the desired phase was obtained. 1 wt% NiO and 1 wt% PVB were added as a sintering aid and binder material, respectively. Dense pellets were achieved by pressing powder in 10 mm dies, followed by sintering at 1400 °C for 5 h.

**Sample Characterization.** X-ray diffraction (XRD) measurements were taken on a Panalytical X'Pert Pro Alpha-1 using CuK $\alpha$ 1 radiation and an XCelerator detector in the range of 20-80 2 $\theta$ . The high-resolution images and diffraction patterns of the samples were characterized using a transmission electron microscope (TEM, JEOL 4000EX). The surface and cross-sectional microstructure, morphology of single cells, and energy dispersive X-ray spectroscopy (EDS) mapping data were examined using a scanning electron microscope (SEM, Hitachi SU8230). To determine electrical conductivity, silver electrodes were affixed to the samples with silver paste (Fuel Cell Materials) and fired to 800 °C for 1 h. The conductivity was measured using an EG&G 263A potentiostat and a Solartron S1255 frequency response analyzer. Ionic transference number was measured by the concentration cell method.<sup>1</sup> The open circuit voltage (OCV) of the concentration cell was measured with one side of the electrolyte pellet (thickness of the pellets are around 1 mm) exposed to 20 sccm humidified H<sub>2</sub> (3% H<sub>2</sub>O) and the other side exposed to 50 sccm humidified air (3 % H<sub>2</sub>O).

**Single Cell Fabrication and Testing.** Half cells with a configuration of Ni-BHCYb172/BHCY172 fuel electrode supporting layer, Ni-BHCYb172/BHCY172 fuel electrode functional layer, and BHCYb/BHCY172 electrolyte layer were fabricated by co-tape casting and co-sintering techniques. Specifically, the BHCYb172/BHCY172 electrolyte powder and the mixture of BHCYb172/BHCY172 and NiO powder (NiO:electrolyte powder = 6:4 by weight) were mixed in solvent to form their respective slurries. The slurries for tape casting were ethanol-

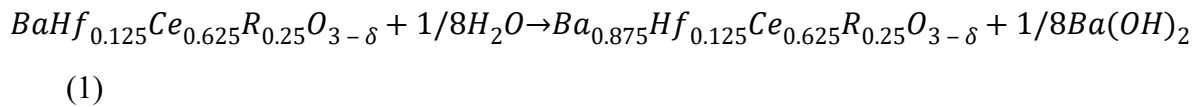
based and contained dispersing agent, binder, plasticizer, and other additives, in addition to powder. The electrolyte layer was cast onto the Mylar film first. After drying, the fuel electrode functional layer was cast on top of the electrolyte layer, followed by the fuel electrode supporting layer. The tri-layer tape was then dried and co-sintered at 1400 °C for 5 h in air. A  $\text{Ba}_{0.9}\text{Co}_{0.7}\text{Fe}_{0.2}\text{Nb}_{0.1}\text{O}_{3-\delta}$  (BCFN) air electrode with an effective area of 0.28 cm<sup>2</sup> was prepared by screen printing the mixture of BCFN powder and terpineol (5 wt% ethyl cellulose) onto the electrolyte layer and fired at 950 °C for 2 h in air. The BCFN powder was synthesized by a solid-state reaction method.<sup>2</sup> Specifically, stoichiometric amounts of  $\text{BaCO}_3$ ,  $\text{Co}_3\text{O}_4$ ,  $\text{Fe}_2\text{O}_3$ , and  $\text{Nb}_2\text{O}_5$  were ball milled and then calcined at 1000 °C for 24 h in air. The as-prepared powder was further ball milled in ethanol for 24 h to get the final product with reduced particle size.

The button cells were mounted on an alumina supporting tube using Ceramabond 552 (Aremco) as sealant for electrochemical performance testing. For the fuel cell test, the fuel electrode was supplied by 20 sccm humidified H<sub>2</sub> (3% H<sub>2</sub>O) and the air electrode was exposed to ambient air. For the electrolysis test, the fuel electrode was fed with 20 sccm humidified H<sub>2</sub> (3% H<sub>2</sub>O) and the air electrode was exposed to 50 sccm humidified air (3% H<sub>2</sub>O, 30% H<sub>2</sub>O, 50% H<sub>2</sub>O). The steam concentration was controlled by a humidification system (Fuel Cell Technologies, Inc.). The cell performance was monitored using an Arbin multichannel electrochemical testing system (MSTAT). Electrochemical impedance spectra (EIS) were acquired using a Solartron 1255 HF frequency response analyzer interfaced with an EG&G PAR potentiostat model 273 A with an AC amplitude of 20 mV in the frequency range from 100 kHz to 0.1 Hz. Faradaic efficiency is defined as the ratio of the measured hydrogen production rate of the electrolysis cell to the theoretical hydrogen production rate calculated from the current density passing through the cell. In our measurements, 20 sccm of 30% H<sub>2</sub>-70% Ar was fed to the fuel electrode and 50 sccm humidified (30% H<sub>2</sub>O) air was fed to the air electrode. Gas chromatography (Shimadzu, Nexis GC-2030) was used to monitor the hydrogen concentration in the effluent gas from the fuel electrode, which was used to calculate the amount of actual hydrogen generated.

**DFT Calculations for H<sub>2</sub>O and CO<sub>2</sub> Tolerance.** All spin-polarized calculations were performed with density functional theory (DFT) method using the Vienna ab initio simulation package (VASP).<sup>3, 4</sup> The projector augment wave (PAW) method was applied with Ba([Kr]5s<sup>2</sup>5p<sup>6</sup>6s<sup>2</sup>), Hf([Kr]5p<sup>6</sup>5d<sup>2</sup>6s<sup>2</sup>), Ce([Ar]4f<sup>1</sup>5s<sup>2</sup>5p<sup>6</sup>5d<sup>1</sup>6s<sup>2</sup>), Yb([Kr]5p<sup>6</sup>6s<sup>2</sup>), Y([Ar]4s<sup>2</sup>4p<sup>6</sup>4d<sup>1</sup>5s<sup>2</sup>),

Er([Kr]5p<sup>6</sup>6s<sup>2</sup>), O([He]2s<sup>2</sup>2p<sup>4</sup>), C([He]2s<sup>2</sup>2p<sup>2</sup>) to solve the interaction between ionic core electrons and valence electrons. The generalized gradient approximation (GGA) with Perdew-Butke-Ernzerhof (PBE) functional was used to take the exchange-correlations into consideration in the Kohn-Sham equations.<sup>5</sup> The energy cutoff and convergence criteria were set as 520 eV and 10<sup>-5</sup> eV, respectively. The structures were relaxed until the force on each atom was less than 0.02 eV Å<sup>-1</sup>. The RMM-DIIS algorithm and the conjugate-gradient were used during the electronic and ionic optimization, respectively. For BaHf<sub>0.1</sub>Ce<sub>0.7</sub>R<sub>0.2</sub>O<sub>3-δ</sub> (R = Yb, Er, and Y), a supercell of BaHf<sub>0.125</sub>Ce<sub>0.625</sub>R<sub>0.25</sub>O<sub>3</sub> with a size of  $2a \times 2a \times 2a$  was constructed, with 8 Ba, 1 Hf, 5 Ce, and 2 R atoms, to approximately describe its properties. A  $3 \times 3 \times 3$   $\Gamma$ -centered  $k$ -point sampling grid was chosen for Brillouin zone integration. All the possible atomic distributions were investigated, where layered-perovskite structure was most energy favorable. The most stable low-index (001) surface was cleaved to elucidate the impact of H<sub>2</sub>O and CO<sub>2</sub> on the BaHf<sub>0.1</sub>Ce<sub>0.7</sub>R<sub>0.2</sub>O<sub>3-δ</sub> surface. An eight-layer  $2a \times 2a$  BaHf<sub>0.125</sub>Ce<sub>0.625</sub>R<sub>0.25</sub>O<sub>3</sub> (001) slab, with the bottom four layers fixed, was built as the substrate for lateral adsorption investigation. A vacuum layer of 15 Å was set to avoid the inter-slab interaction between two neighboring cells. Dipole correction was applied and a  $2 \times 2 \times 1$   $\Gamma$ -centered  $k$ -point sampling grid was chosen for the Brillouin zone integration. Bader charges were also calculated to illustrate the charge transfer between CO<sub>2</sub> and BaHf<sub>0.125</sub>Ce<sub>0.625</sub>R<sub>0.25</sub>O<sub>3</sub> (001) surface (Table S2).

The potential barium hydroxide formation reaction is described as



and the Gibbs free energy of it is calculated as

$$\Delta G = 1/8G(\text{Ba}(\text{OH})_2) + G(\text{Barium\_defect}) - 1/8G(\text{H}_2\text{O}) - G(\text{perfect}) \quad (2)$$

where  $G(\text{Ba}(\text{OH})_2)$ ,  $G(\text{Barium\_defect})$ ,  $G(\text{H}_2\text{O})$ , and  $G(\text{perfect})$  are the Gibbs free energy of Ba(OH)<sub>2</sub>, bulk structure with one eighth barium atom removed, H<sub>2</sub>O, and perfect bulk structure, respectively. The value of  $G(\text{Ba}(\text{OH})_2)$  and  $G(\text{H}_2\text{O})$  are extracted from NIST-JANAF thermochemical tables.<sup>6</sup> The zero-energy potential and entropy corrections aren't taken into consideration for the barium defect and perfect bulk structure, since they share similar vibrational frequency.

To emphasize the difference introduced by different rare earth dopants, the adsorbed position is chosen to be directly above the oxygen atom to which the acceptor dopant is attached. The H<sub>2</sub>O adsorption energy is defined as

$$E_{ads} = E(H_2O - slab) - E(slab) - E(H_2O) \quad (3)$$

where  $E(H_2O - slab)$  is the total energy of the surface with adsorbed H<sub>2</sub>O,  $E(slab)$  is the total energy of the slab without H<sub>2</sub>O adsorption, and  $E(H_2O)$  is the total energy of free H<sub>2</sub>O. The CO<sub>2</sub> adsorption energy is defined as

$$E_{ads} = E(CO_2 - slab) - E(slab) - E(CO_2) \quad (4)$$

where  $E(CO_2 - slab)$  is the total energy of the surface with adsorbed CO<sub>2</sub>,  $E(slab)$  is the total energy of the slab without CO<sub>2</sub> adsorption, and  $E(CO_2)$  is the total energy of free CO<sub>2</sub>.

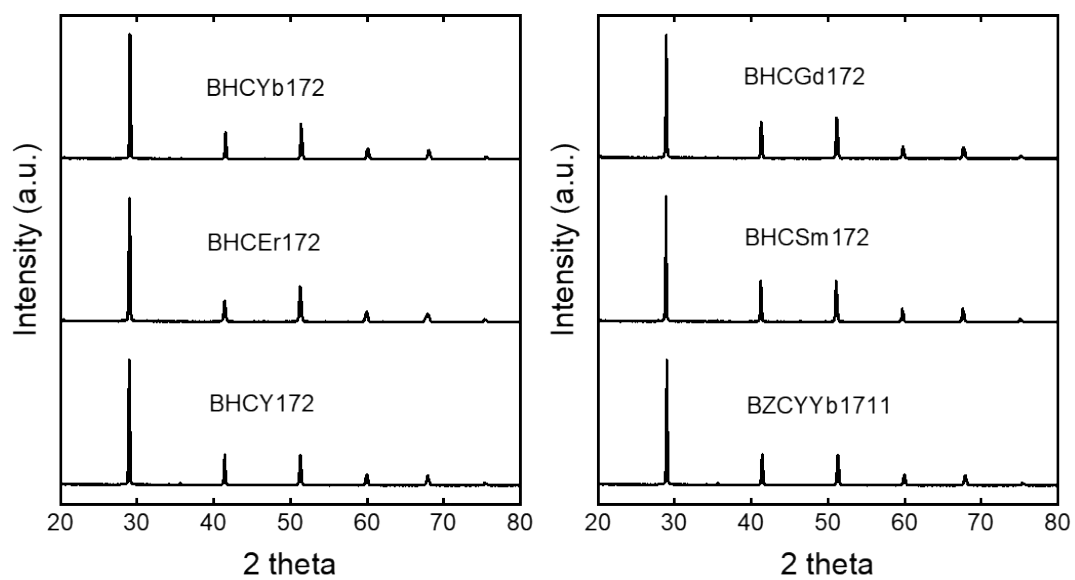


*Fig S1. XRD patterns of BHCRI172 (R = Yb, Er, Y, Gd, Sm) and BZCYYb1711.*

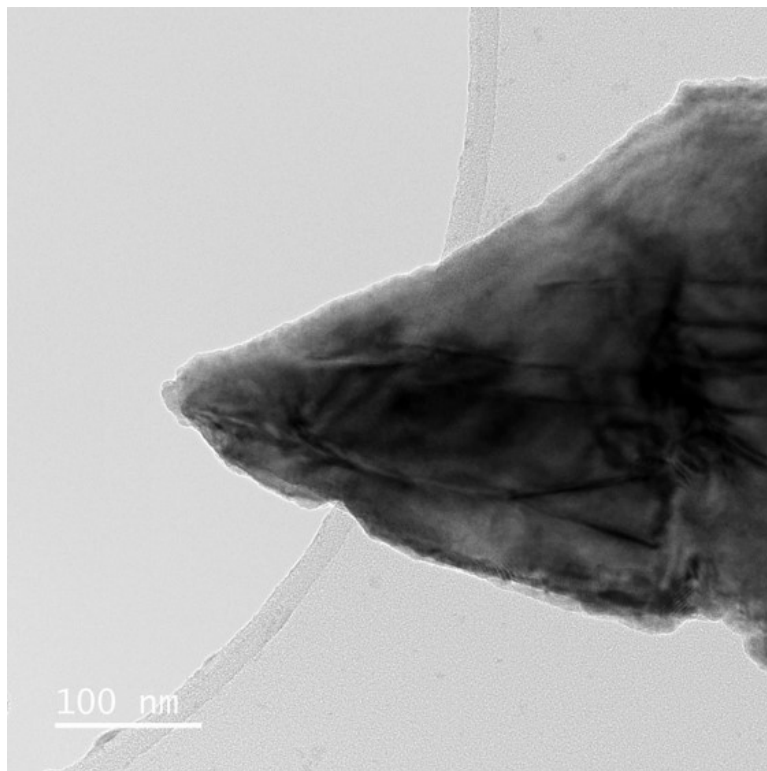


*Fig S2. TEM image of BHCYb172.*

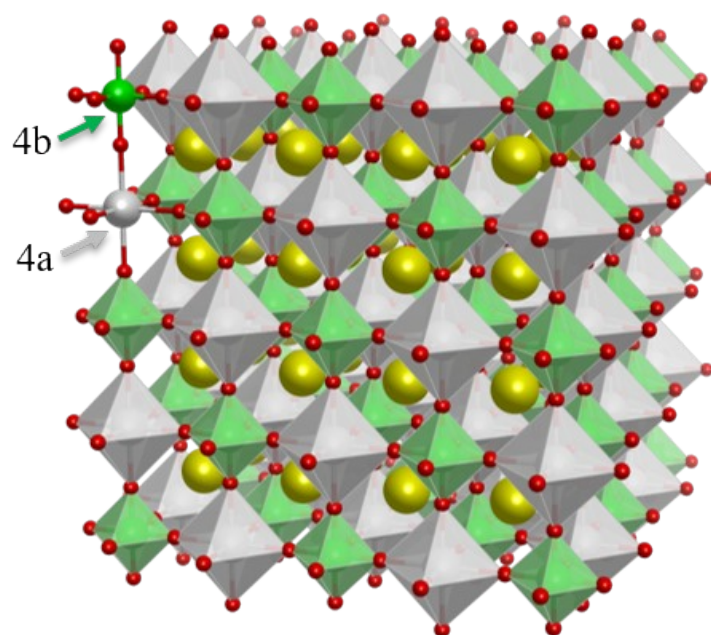


*Fig S3. Crystal structure of cubic double perovskite BHfYb172 ( $Fm\bar{3}m$ ) Yellow balls: Ba sites. Grey balls: Ce rich 4a sites. Green balls: Ce/Hf/Yb containing 4b sites. Red balls: O sites.*

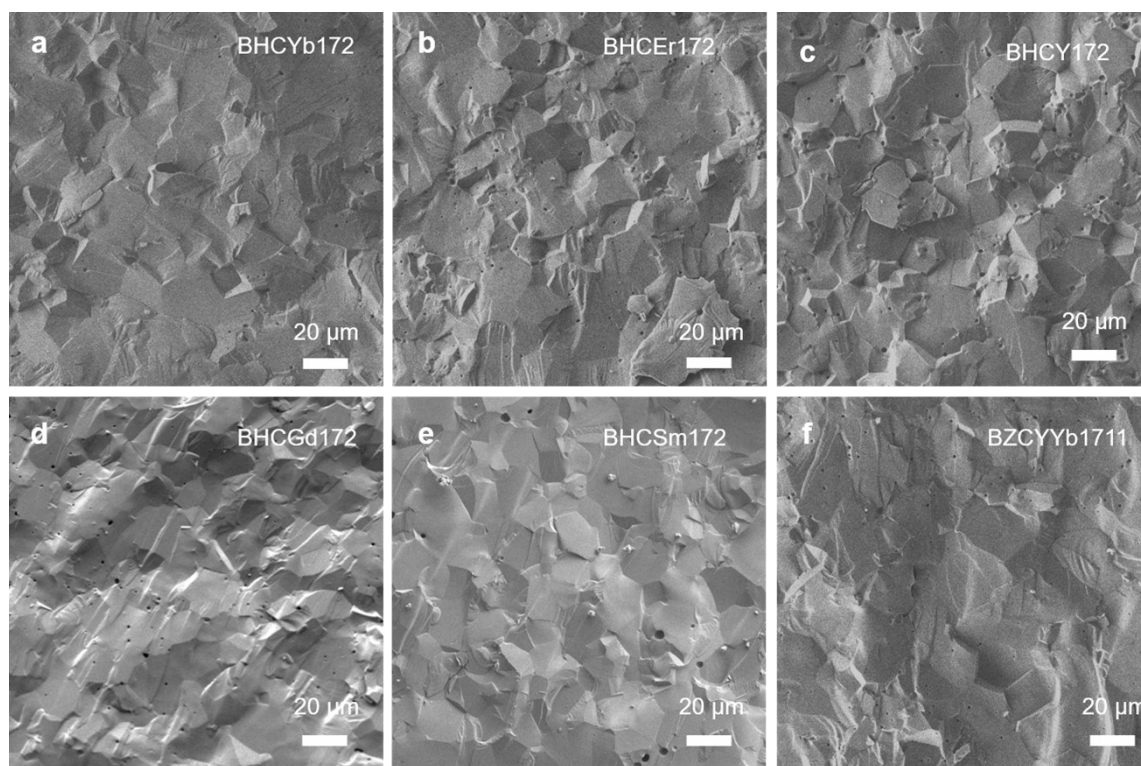


*Fig S4. Cross-sectional SEM images of a) BHCYb172, b) BHCEr172, c) BHCY172, d) BHCGd172, e) BHCSm172, and e) BZCYYb1711 pellets.*

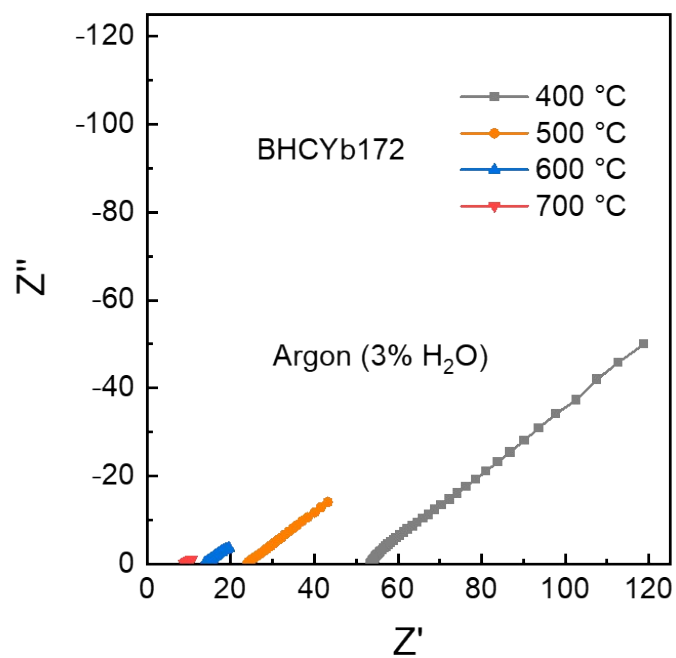


Fig S5. Nyquist plot of the impedance results of BHCYb172 in Ar with 3% H<sub>2</sub>O.

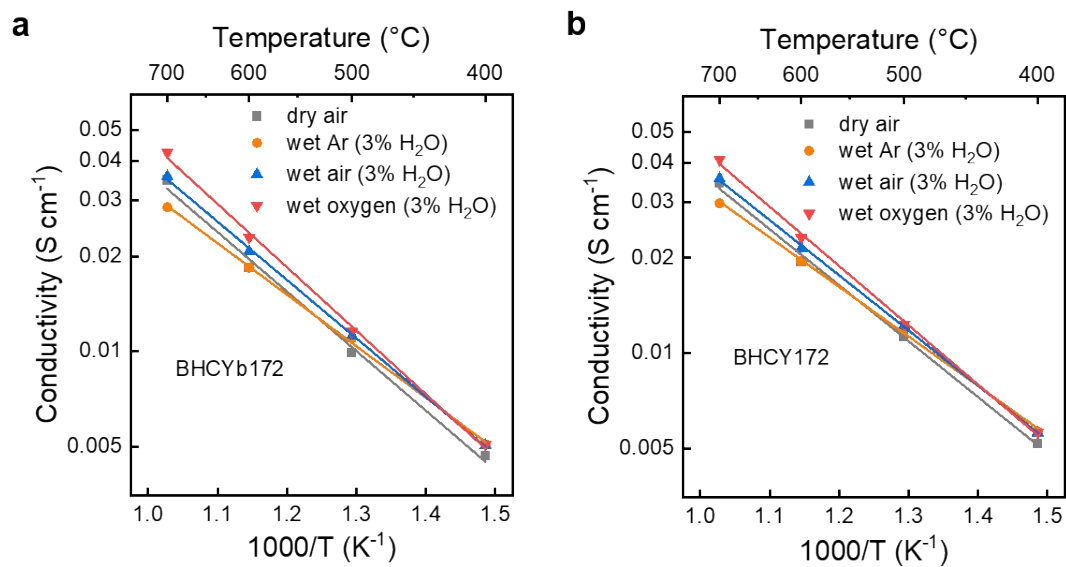


Fig S6. Conductivity of a) BHCYb172 and b) BHCY172 as a function of temperature under various atmospheres.

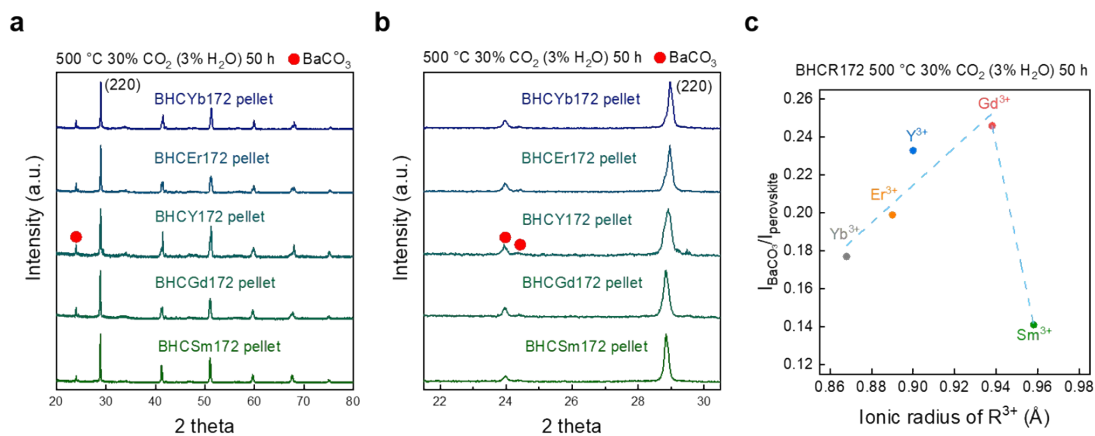


Fig S7. a) Full and b) magnified view of XRD patterns of BHCR172 ( $R = Yb, Er, Y, Gd, Sm$ ) pellets after exposure to 30% CO<sub>2</sub> and 3% H<sub>2</sub>O in Ar at 500 °C for 50 h. c) Intensity ratio between BaCO<sub>3</sub> and perovskite (220) peaks of BHCR172 as a function of the ionic radius of R<sup>3+</sup>.

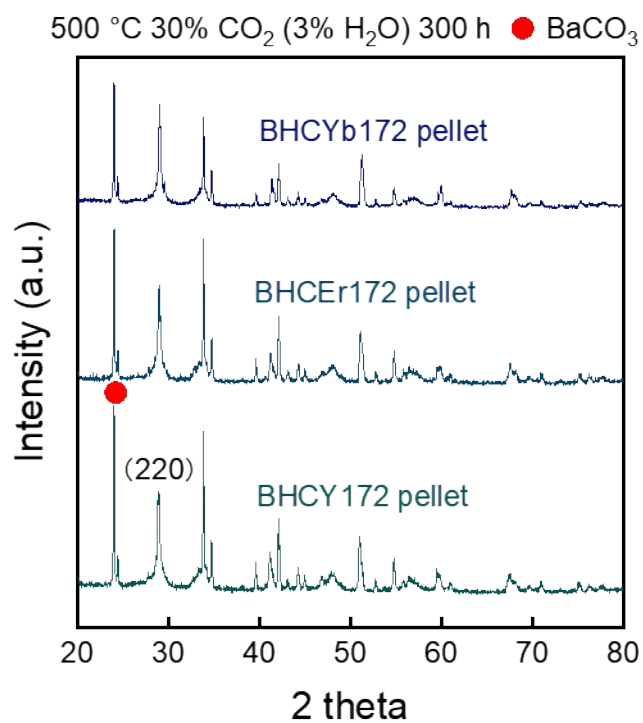


Fig S8. XRD patterns of BHCR172 ( $R = \text{Yb, Er, Y}$ ) pellets after exposure to 30% CO<sub>2</sub> and 3% H<sub>2</sub>O in Ar at 500 °C for 300 h.

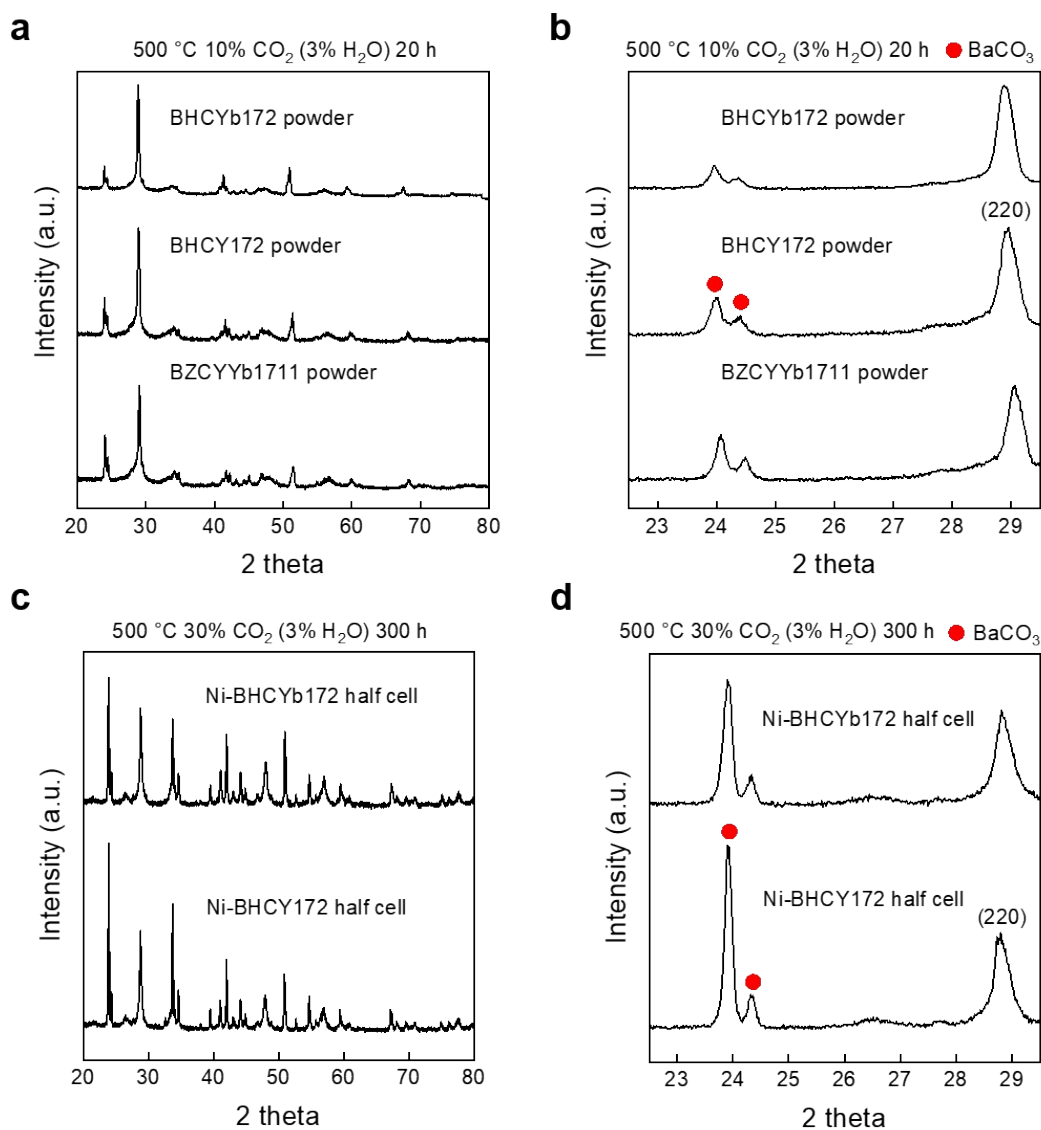
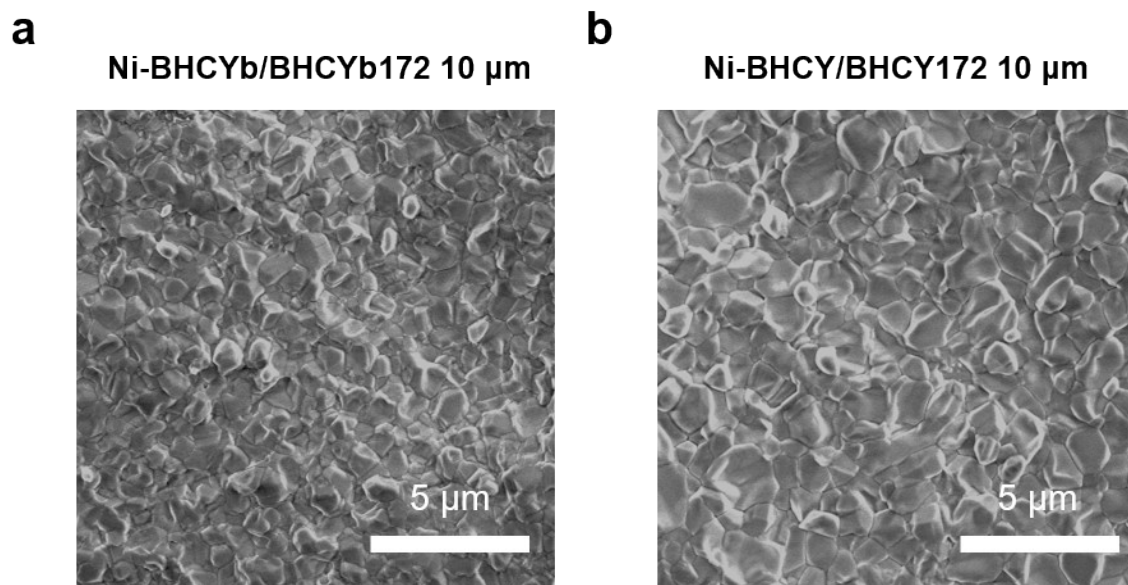
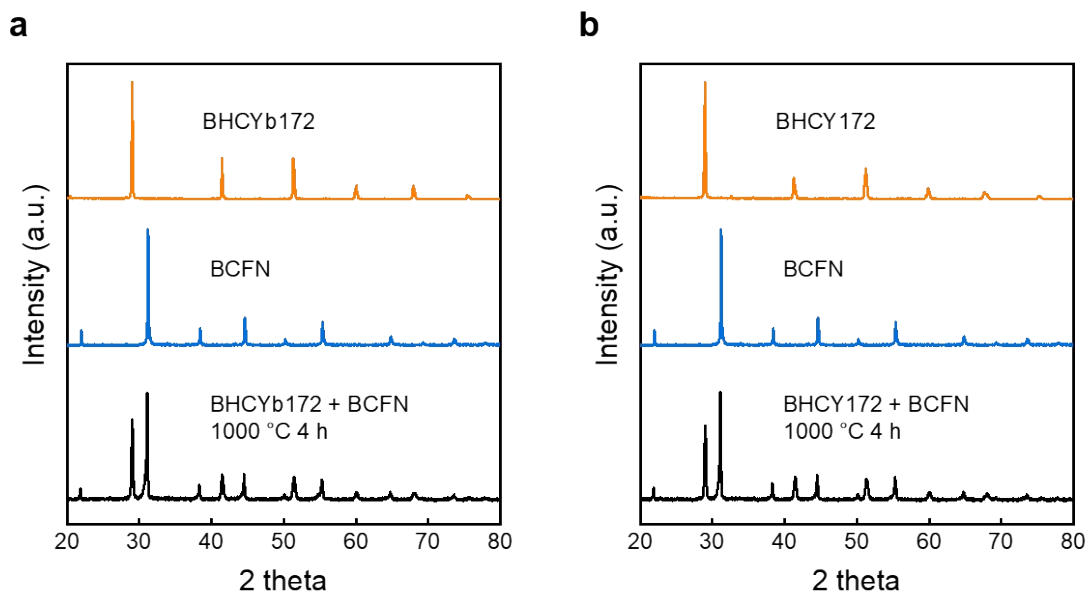


Fig S9. a) Full and b) magnified view of XRD patterns of BHCYb172, BHCY172, and BZCYYb1711 powders after exposure to 10% CO<sub>2</sub> and 3% H<sub>2</sub>O in Ar at 500 °C for 20 h. c) Full and d) magnified view of XRD patterns of the electrolyte surface of Ni-BHCYb/BHCYb172 and Ni-BHCY/BHCY172 fuel electrode-supported half cells after exposure to 30% CO<sub>2</sub> and 3% H<sub>2</sub>O in Ar at 500 °C for 300 h.



*Fig S10. SEM images of the electrolyte surface of a) Ni-BHCYb/BHCYb172 and b) Ni-BHCY/BHCY172 fuel electrode-supported half cells after exposure to 30% CO<sub>2</sub> and 3% H<sub>2</sub>O in Ar at 500 °C for 300 h.*



*Fig S11. XRD patterns of a) BHCYb172 and b) BHCY172 after calcining with BCFN at 1000 °C for 4 h.*

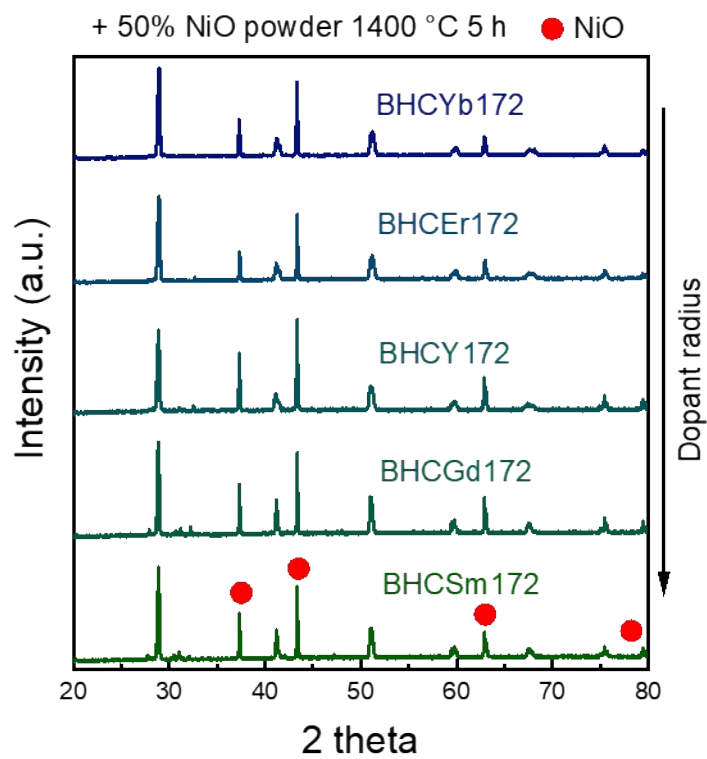


Fig S12. XRD patterns of BHCRI172 ( $R = \text{Yb}, \text{Er}, \text{Y}, \text{Gd}, \text{Sm}$ ) after firing with NiO at 1400 °C for 5 h.

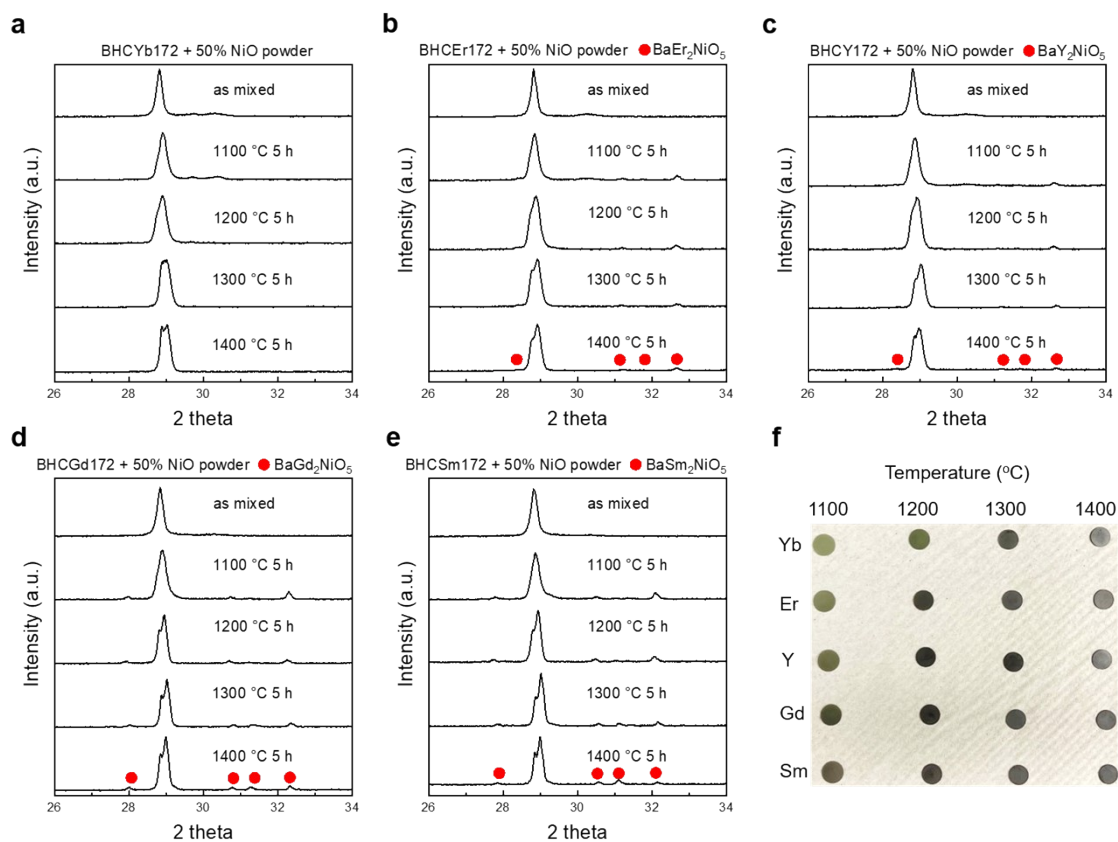
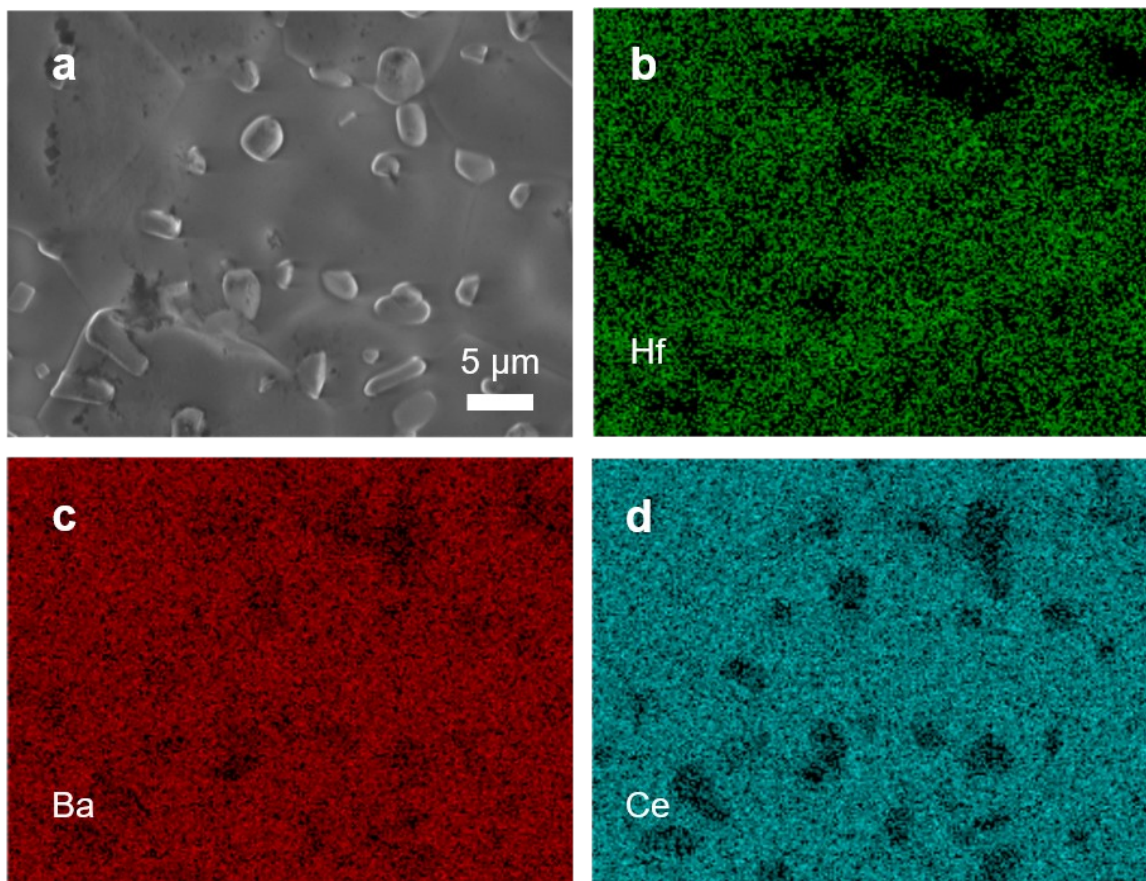
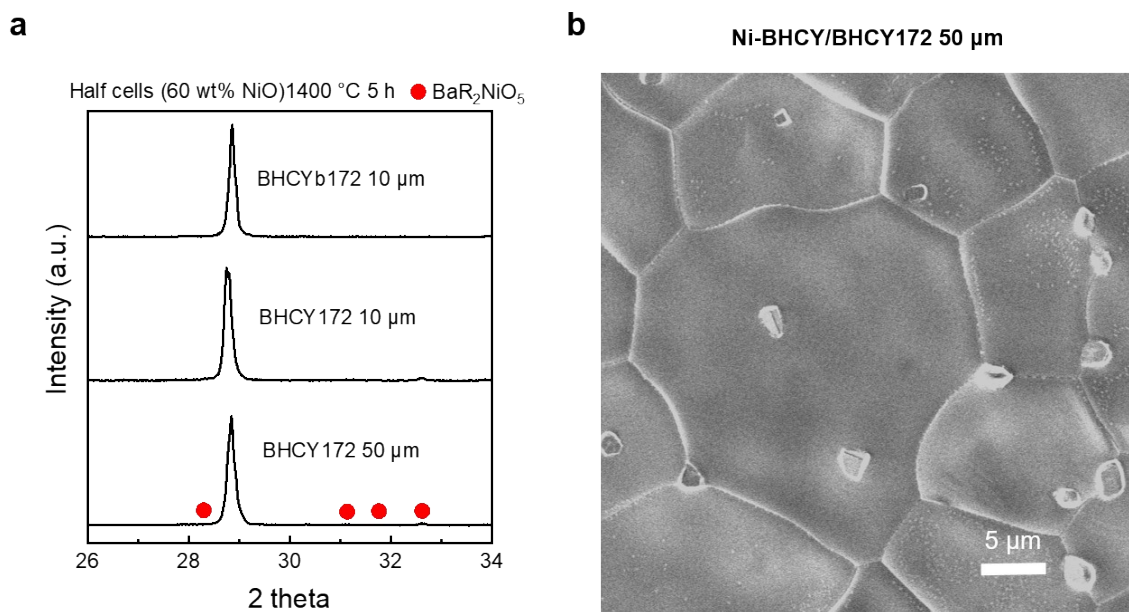


Fig S13. XRD patterns of a) BHCYb172, b) BHCEr172, c) BHCY172, d) BHCGd172, and e) BHCSm172 after firing with NiO at various temperatures. f) Images of BHCr172 samples after firing with NiO at various temperatures.

**Ni-BHCY/BHCY172 10  $\mu\text{m}$** 

*Fig S14. a) SEM image of the electrolyte surface of a Ni-BHCY/BHCY172 fuel electrode-supported half cell (electrolyte thickness = 10  $\mu\text{m}$ ) after firing at 1400  $^{\circ}\text{C}$  for 5 h. b-d) EDS mapping of the corresponding elements.*



*Fig S15. a) XRD patterns of the electrolyte surface of Ni-BHCYb/BHCYb172 and Ni-BHCY/BHCY172 fuel electrode-supported half cells with various electrolyte thicknesses after firing at 1400 °C for 5 h. b) SEM image of the electrolyte surface of a Ni-BHCY/BHCY172 fuel electrode-supported half cell (electrolyte thickness = 50 μm) after firing at 1400 °C for 5 h.*

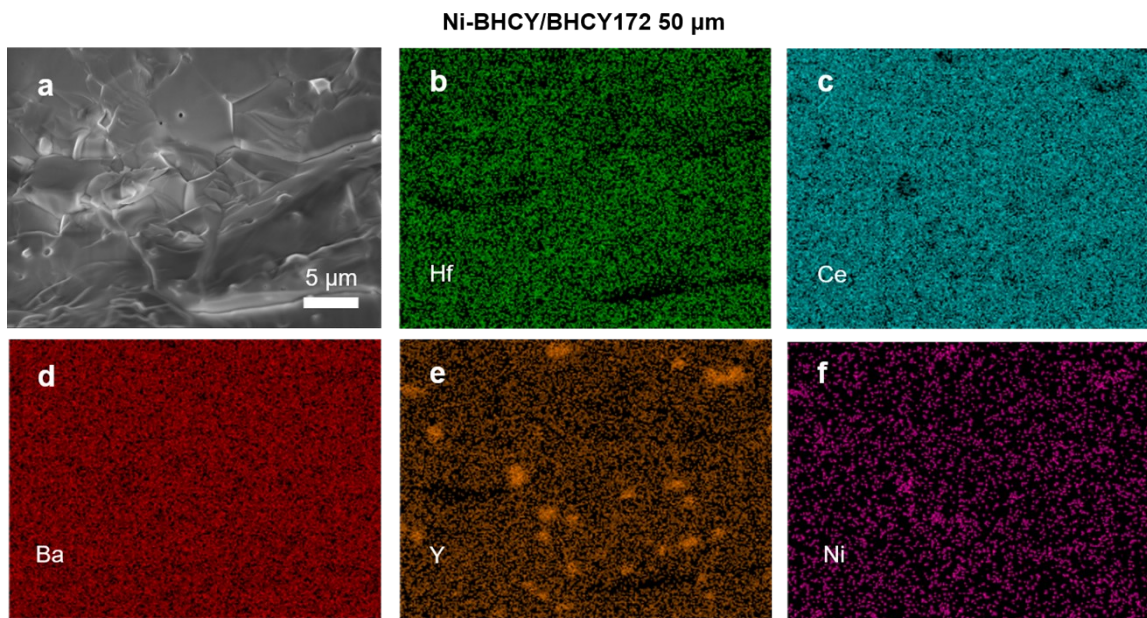


*Fig S16. a) Cross-sectional SEM image of a Ni-BHCY/BHCY172 fuel electrode-supported half cell (electrolyte thickness = 50  $\mu\text{m}$ ) after firing at 1400  $^{\circ}\text{C}$  for 5 h. b-f) EDS mapping of the corresponding elements.*

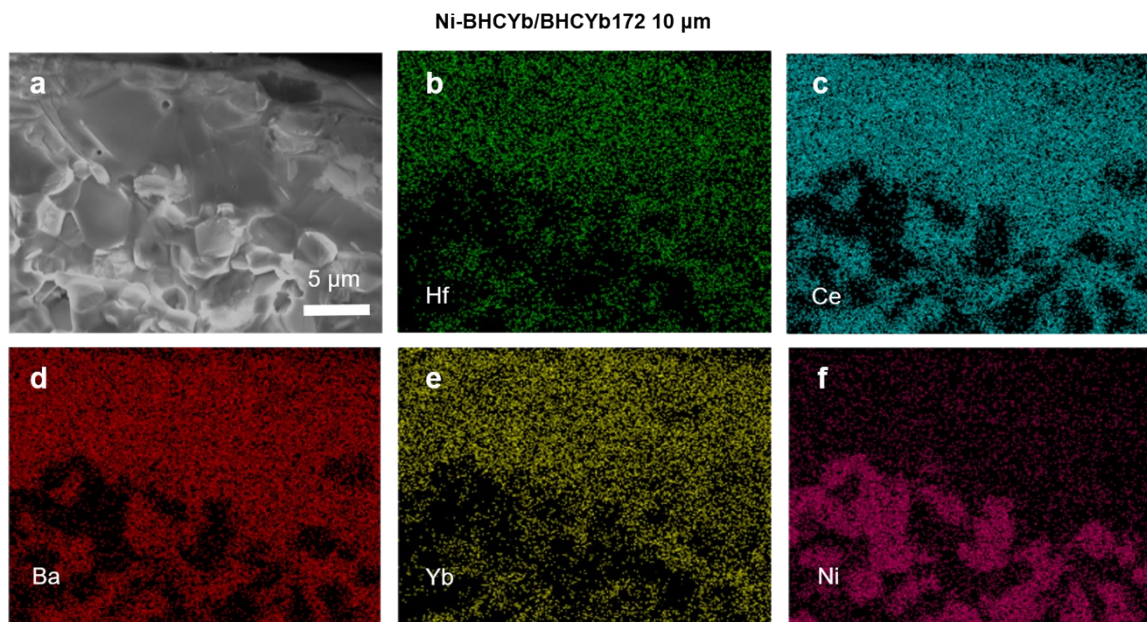


*Fig S17. a) Cross-sectional SEM image of a Ni-BHCYb/BHCYb172 fuel electrode-supported half cell (electrolyte thickness = 10  $\mu\text{m}$ ) after firing at 1400  $^{\circ}\text{C}$  for 5 h. b-f) EDS mapping of the corresponding elements.*

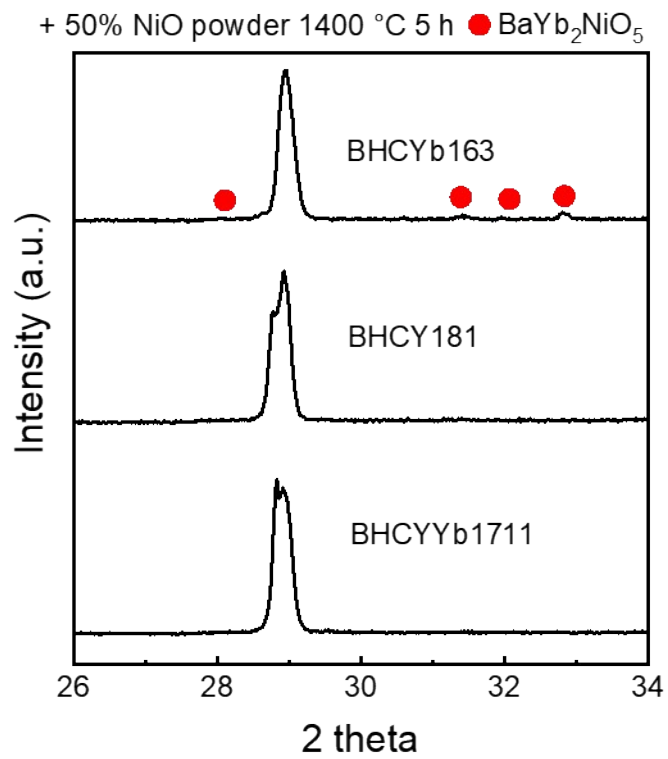


Fig S18. XRD patterns of BHCYb163, BHCY181, and BHCYYb1711 after firing with NiO at 1400 °C for 5 h.

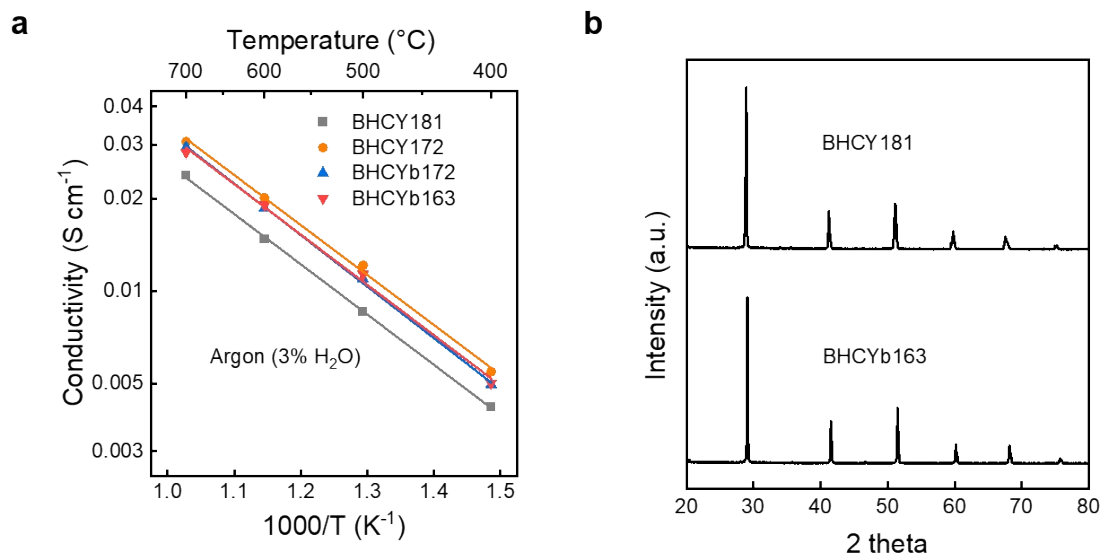


Fig S19. a) Conductivity of BHCY181, BHCY172, BHCYb172, and BHCYb163 as a function of temperature. b) XRD patterns of BHCY181 and BHCYb163.

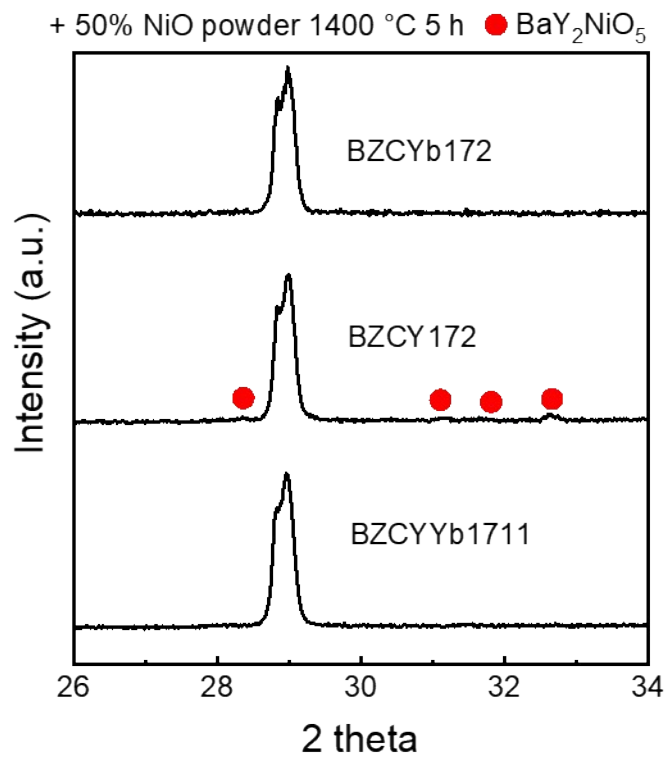


Fig S20. XRD patterns of BZCYb172, BZCY172, and BZCYYb1711 after firing with NiO at 1400 °C for 5 h.

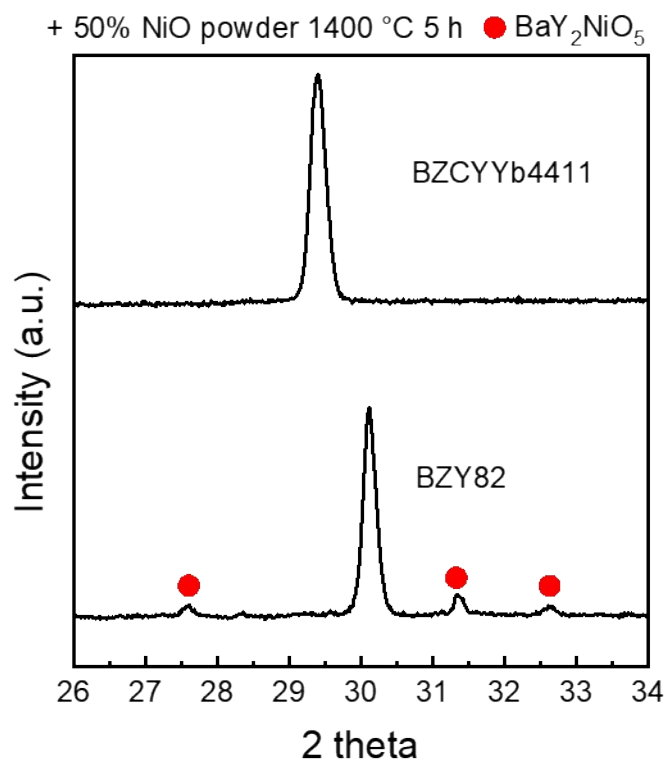
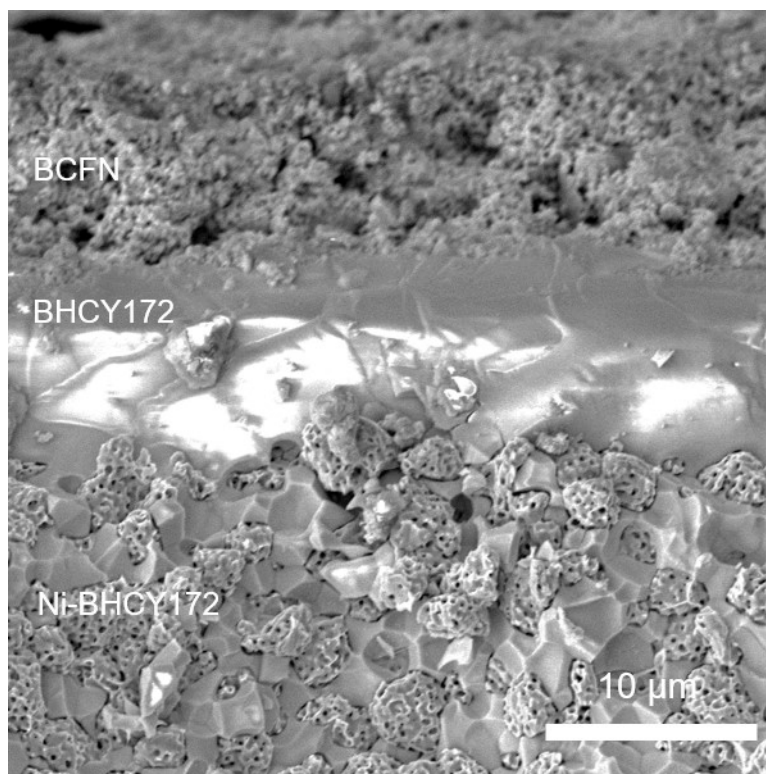


Fig S21. XRD patterns of BZCYYb4411 and BZY82 after firing with NiO at 1400 °C for 5 h.



*Fig S22. Cross-sectional SEM image of a single cell with the configuration of Ni-BHCOY172/BHCOY172/BCFN.*

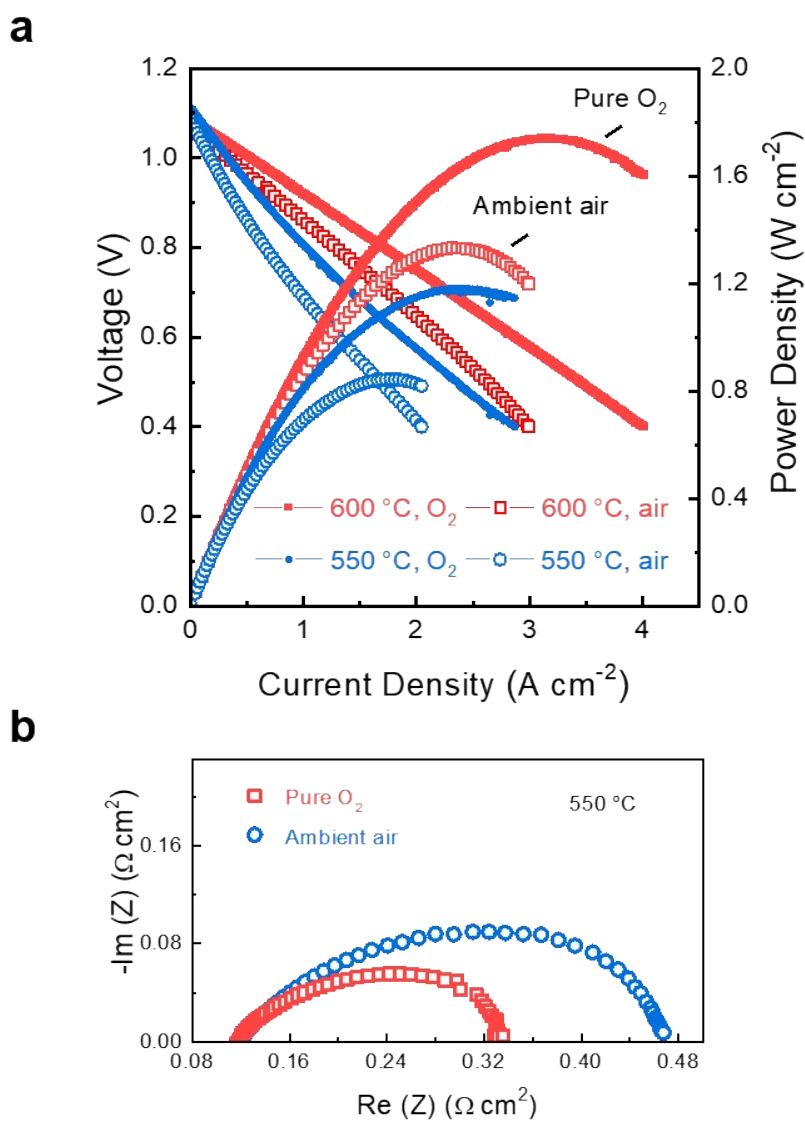


Fig S23. a) I-V-P curves and b) Nyquist plot of the impedance results of a BHCYb172-based single cell measured in the fuel cell mode at 550-600 °C with  $H_2$  (3%  $H_2O$ , 20 sccm) in the fuel electrode and ambient air or pure oxygen (50 sccm) in the air electrode.

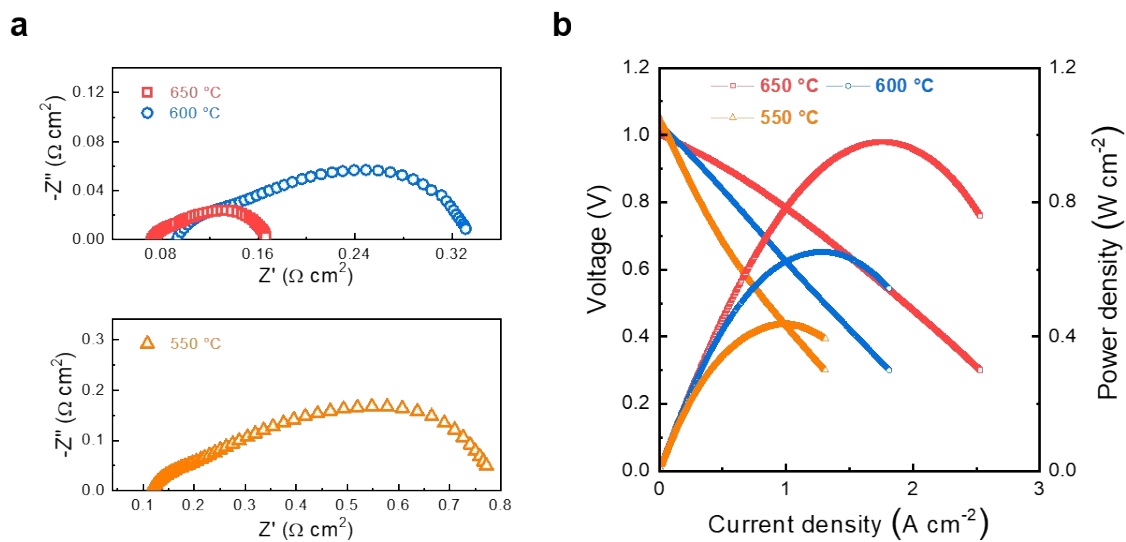
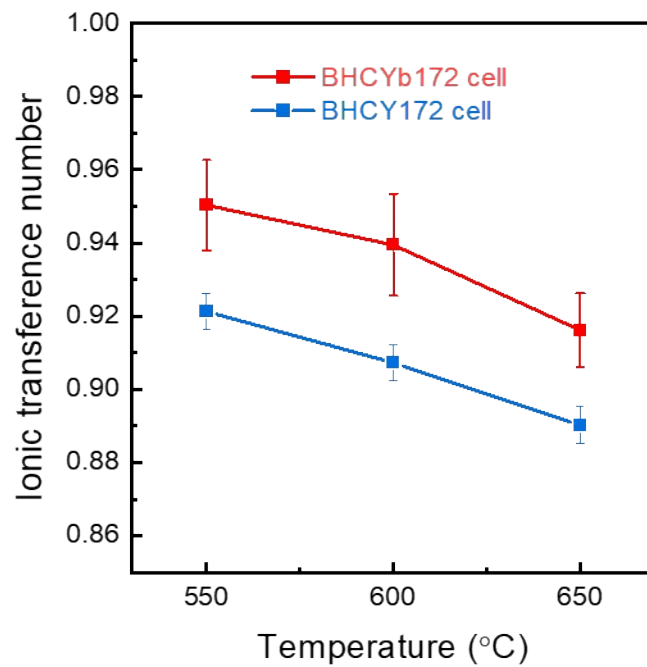


Fig S24. a) Nyquist plot of the impedance results under open circuit conditions and b) I-V-P curves of a BHCY172-based single cell operated at 550-650 °C using wet  $\text{H}_2$  (3%  $\text{H}_2\text{O}$ ) as the fuel and ambient air as the oxidant.



*Fig S25. Comparison of the ionic transference number (calculated by the ratio of the measured OCV to the theoretical Nernst potential) between BHCYb172- and BHCY172-based single cells at 550-650 °C.*

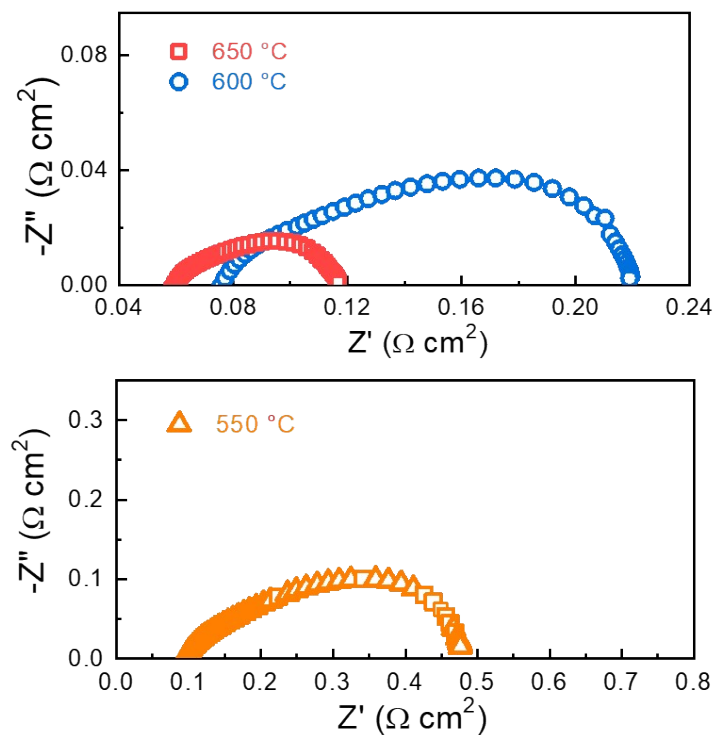


Fig S26. Nyquist plot of the impedance results of a BHCYb172-based single cell operated at 550-650 °C using wet  $\text{H}_2$  (3%  $\text{H}_2\text{O}$ ) as the fuel and ambient air as the oxidant under open circuit conditions.

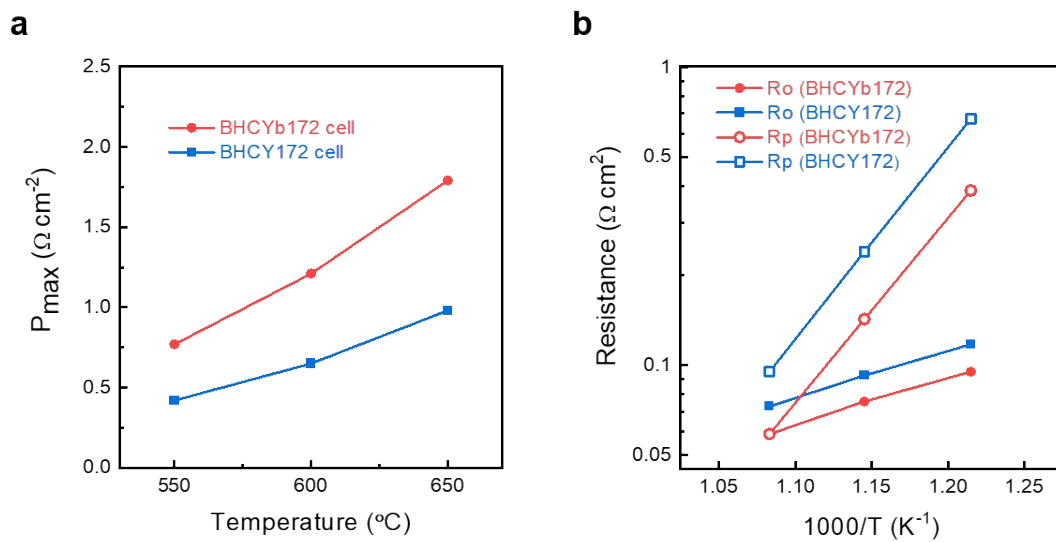


Fig S27. Comparison of a) peak power density and b) ohmic resistance ( $R_o$ ) and polarization resistance ( $R_p$ ) between BHCYb172- and BHCY172-based single cells at 550-650  $^{\circ}C$ .

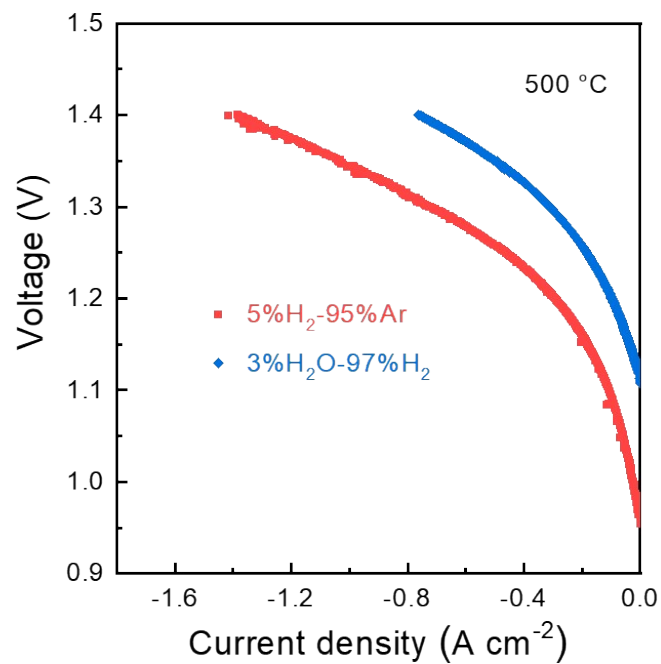
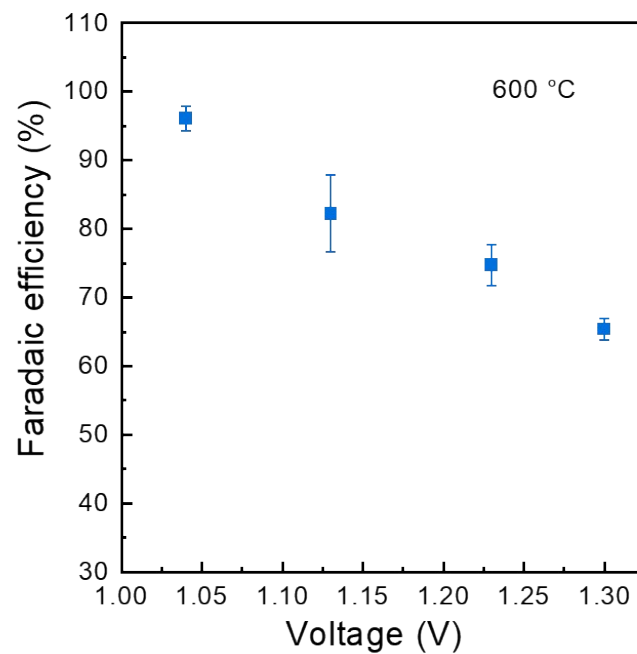
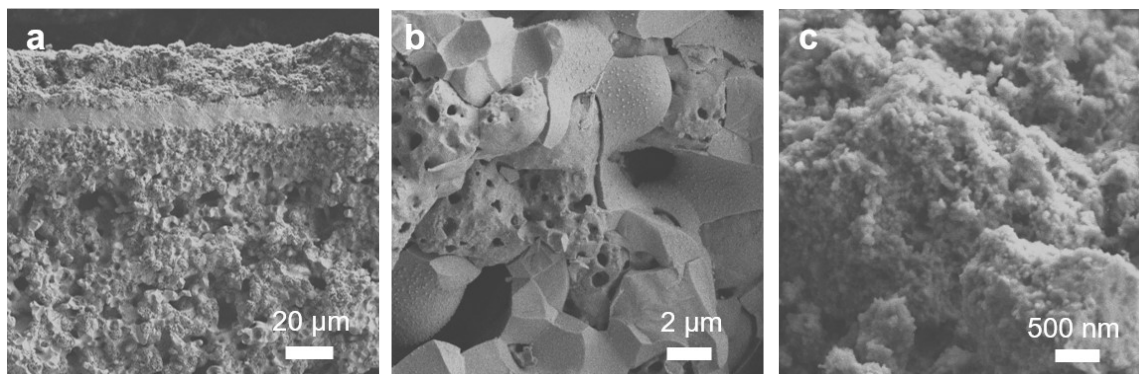


Fig S28. I-V curves of a Ni-BHCYb172/BHCYb172/BCFN single cell measured in the electrolysis mode at 500 °C with H<sub>2</sub> (3% H<sub>2</sub>O) or 5% H<sub>2</sub>-95% Ar in the fuel electrode and air (3% H<sub>2</sub>O) in the air electrode.



*Fig S29. Faradaic efficiency of a BHCYb172-based single cell as a function of applied cell voltage in the electrolysis mode at 600 °C with 30% H<sub>2</sub>-70% Ar in the fuel electrode and air (30% H<sub>2</sub>O) in the air electrode.*



*Fig S30. Cross-sectional SEM image of a) Ni-BHCYb/BHCYb172/BCFN single cell, b) fuel electrode, and c) air electrode after the long-term stability test at 500 °C and  $-0.5 \text{ A cm}^{-2}$  for over 1400 h with  $\text{H}_2$  (3%  $\text{H}_2\text{O}$ ) in the fuel electrode and air (3%  $\text{H}_2\text{O}$ ) in the air electrode.*

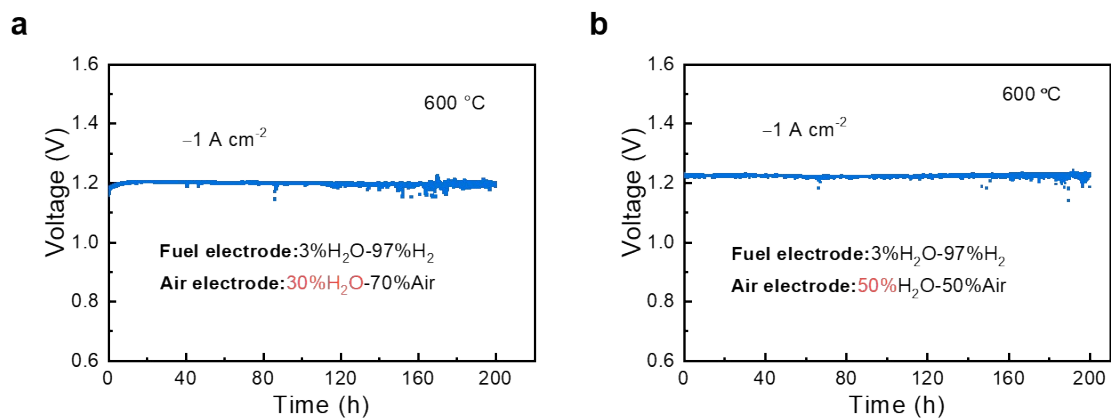


*Fig S31. Long-term stability of the electrolysis cell at 600 °C and -1 A cm<sup>-2</sup> with a) 30% H<sub>2</sub>O and b) 50% H<sub>2</sub>O on the air electrode side.*

**Table S1.** Summary of electrolyte, electrolyte thickness, fuel electrode/air electrode materials, and peak power density (PPD) measured in air/oxygen at 600 °C for recent proton-conducting solid oxide fuel cells.

Electrolyte	Thickness ( $\mu\text{m}$ )	Fuel electrode/ Air electrode	PPD ( $\text{W cm}^{-2}$ )	Reference
BCZY3*	~5	Ni-BCZY3/BSCF*	1.3 (air)	7
BZCYYb4411*	~15	Ni-BZCYY4411/PBSCF*	1.1 (air)	8
BZCYYb4411	~15	Ni-BZCYY4411/PBSCF	~1.0 (air)	9
BZCYYb	~30	Ni-BZCYYb/BCFZY*	~0.65 (air)	10
BZCYYb	~10	Ni-BZCYYb/PBCC*	1.06 (ambient Air)	11
BZCYYb	~15	Ni-BZCYYb/NBSCF*	0.69 (air)	12
BZCYYb4411	10	Ni-BZCYYb4411/PNC*	0.61 (air)	13
BZCYYb	~10	Ni-BZCYYb/BCO*-LSCF	1.16 (ambient Air)	14
BZCYYb	~16	Ni-BZCYYb/BCCY*	0.74 (ambient Air)	15
BZCYYb	~15	Ni-BZCYYb/GCCCO*	1.16 (ambient Air)	16
BZCYYb4411	~7	Ni-BZCYYb4411/PBSCF	1.47 (ambient Air)	17
BZCYYb	26	Ni-BZCYYb/SCFN*	0.53 (ambient Air)	18
BZCYYb	16	Ni-BZCYYb/3D PBSCF	1.21 (pure O <sub>2</sub> )	19
BZCYYb	~16	Ni-BZCYYb/3D PNC	1.6 (pure O <sub>2</sub> )	20
BHCYb172	~10	NiO-BHCYb172/BCFN	1.74 (pure O <sub>2</sub> ) 1.33 (ambient Air)	<b>This work</b>

\*BCZY3 ( $\text{BaCe}_{0.55}\text{Zr}_{0.3}\text{Y}_{0.15}\text{O}_{3-\delta}$ ), BSCF ( $\text{Ba}_{0.5}\text{Sr}_{0.5}\text{Co}_{0.8}\text{Fe}_{0.2}\text{O}_3$ ), BZCYYb4411 ( $\text{BaZr}_{0.4}\text{Ce}_{0.4}\text{Y}_{0.1}\text{Yb}_{0.1}\text{O}_3$ ), PBSCF ( $\text{PrBa}_{0.5}\text{Sr}_{0.5}\text{Co}_{1.5}\text{Fe}_{0.5}\text{O}_{5+\delta}$ ), BCFZY ( $\text{BaCo}_{0.4}\text{Fe}_{0.4}\text{Zr}_{0.1}\text{Y}_{0.1}\text{O}_{3-d}$ ), PBCC ( $\text{PrBa}_{0.8}\text{Ca}_{0.2}\text{Co}_2\text{O}_{5+\delta}$ ), NBSCF ( $\text{NdBa}_{0.5}\text{Sr}_{0.5}\text{Co}_{1.5}\text{Fe}_{0.5}\text{O}_{5+\delta}$ ), PNC ( $\text{PrNi}_{0.5}\text{Co}_{0.5}\text{O}_{3-\delta}$ ), BCO ( $\text{BaCoO}_{3-\delta}$ ), BCCY ( $\text{BaCo}_{0.7}(\text{Ce}_{0.8}\text{Y}_{0.2})_{0.3}\text{O}_{3-\delta}$ ), GCCCO ( $\text{Gd}_{0.3}\text{Ca}_{2.7}\text{Co}_{3.82}\text{Cu}_{0.18}\text{O}_{9-\delta}$ ), SCFN ( $\text{Sr}_{0.9}\text{Ce}_{0.1}\text{Fe}_{0.8}\text{Ni}_{0.2}\text{O}_{3-\delta}$ ).

**Table S2.** Bader charges information regarding the charge transfer between CO<sub>2</sub> and BaHf<sub>0.125</sub>Ce<sub>0.625</sub>R<sub>0.25</sub>O<sub>3</sub> (001) surface.

Carbonate	Yb	Er	Y
O1	-1.23733	-1.23267	-1.23886
O2	-1.23019	-1.23903	-1.24485
C	2.08229	2.07896	2.10405
C-O1	1.28144	1.29312	1.28625
C-O2	1.29397	1.28311	1.29329
C-O3	1.34056	1.34038	1.33562

## Reference

1. Y. Du and A. S. Nowick, *Solid State Ionics*, 1996, **91**, 85-91.
2. C. H. Yang, F. Zhao, F. L. Chen and M. L. Liu, *Int J Hydrogen Energ*, 2014, **39**, 8431-8436.
3. P. E. Blochl, *Phys Rev B*, 1994, **50**, 17953-17979.
4. G. Kresse and J. Furthmuller, *Comp Mater Sci*, 1996, **6**, 15-50.
5. J. P. Perdew, K. Burke and M. Ernzerhof, *Phys Rev Lett*, 1996, **77**, 3865-3868.
6. R. R. Zarr, G. R. Dalton and S. M. Fioravante, *Therm Cond*, 2000, **25**, 259-265.
7. H. An, H. W. Lee, B. K. Kim, J. W. Son, K. J. Yoon, H. Kim, D. Shin, H. I. Ji and J. H. Lee, *Nat Energy*, 2018, **3**, 870-875.
8. S. Choi, C. J. Kucharczyk, Y. G. Liang, X. H. Zhang, I. Takeuchi, H. I. Ji and S. M. Haile, *Nat Energy*, 2018, **3**, 202-210.
9. S. Choi, T. C. Davenport and S. M. Haile, *Energ Environ Sci*, 2019, **12**, 206-215.
10. C. C. Duan, J. H. Tong, M. Shang, S. Nikodemski, M. Sanders, S. Ricote, A. Almansoori and R. O'Hayre, *Science*, 2015, **349**, 1321-1326.
11. Y. C. Zhou, E. Z. Liu, Y. Chen, Y. C. Liu, L. Zhang, W. L. Zhang, Z. Y. Luo, N. Kane, B. Zhao, L. Soule, Y. H. Niu, Y. Ding, H. P. Ding, D. Ding and M. L. Liu, *Acs Energy Lett*, 2021, **6**, 1511-1520.
12. J. Kim, S. Sengodan, G. Kwon, D. Ding, J. Shin, M. L. Liu and G. Kim, *Chemsuschem*, 2014, **7**, 2811-2815.
13. H. P. Ding, W. Wu, C. Jiang, Y. Ding, W. J. Bian, B. X. Hu, P. Singh, C. J. Orme, L. C. Wang, Y. Y. Zhang and D. Ding, *Nat Commun*, 2020, **11**.
14. Y. C. Zhou, W. L. Zhang, N. Kane, Z. Y. Luo, K. Pei, K. Sasaki, Y. M. Choi, Y. Chen, D. Ding and M. L. Liu, *Adv Funct Mater*, 2021, **31**.
15. Y. S. Song, Y. B. Chen, W. Wang, C. Zhou, Y. J. Zhong, G. M. Yang, W. Zhou, M. L. Liu and Z. P. Shao, *Joule*, 2019, **3**, 2842-2853.
16. M. Saqib, I. G. Choi, H. Bae, K. Park, J. S. Shin, Y. D. Kim, J. I. Lee, M. Jo, Y. C. Kim, K. S. Lee, S. J. Song, E. D. Wachsman and J. Y. Park, *Energ Environ Sci*, 2021, **14**, 2472-2484.
17. M. Choi, J. Paik, D. Kim, D. Woo, J. Lee, S. J. Kim, J. Lee and W. Lee, *Energ Environ Sci*, 2021, **14**, 6476-6483.
18. Y. F. Song, J. P. Liu, Y. H. Wang, D. Q. Guan, A. Seong, M. Z. Liang, M. J. Robson, X. D. Xiong, Z. Q. Zhang, G. Kim, Z. P. Shao and F. Ciucci, *Adv Energy Mater*, 2021, **11**.
19. W. J. Bian, W. Wu, Y. P. Gao, J. Y. Gomez, H. P. Ding, W. Tang, M. Zhou and D. Ding, *Adv Funct Mater*, 2021, **31**.
20. W. J. Bian, W. Wu, B. M. Wang, W. Tang, M. Zhou, C. R. Jin, H. P. Ding, W. W. Fan, Y. H. Dong, J. Li and D. Ding, *Nature*, 2022, **604**.